Interplay between solidification microsegregation and complex precipitation in a γ/γ' cobalt-based superalloy elaborated by Directed Energy Deposition

Thibaut Froeliger, Arthur Després, Louise Toualbi, Didier Locq, Muriel Veron, Guilhem Martin, Rémy Dendievel

Interplay between solidification microsegregation and complex precipitation in a γ/γ’ cobalt-based superalloy elaborated by Directed Energy Deposition

Authors

Thibaut Froeliger[1*], Arthur Després[2], Louise Toualbi[1], Didier Locq[1], Muriel Veron[2], Guilhem Martin[2], Rémy Dendievel[2]

[1] DMAS, ONERA, Université Paris Saclay, F-92322 Châtillon, France

[2] Univ. Grenoble Alpes, CNRS, Grenoble INP, SIMaP, Grenoble F-38000, France

[*] thibaut.froeliger@onera.fr (+33 1 46 73 48 92)

Abstract

This study examines the segregations and the precipitation appearing during the solidification path of a Co-Ni-Al-W-Ta-Ti-Cr γ/γ’ cobalt-based superalloy processed by directed energy deposition (DED). Observations reveal characteristic elements partitioning in the liquid during additive manufacturing. Due to this microsegregation, complex multiphase precipitation occurs and the various precipitates are identified and characterized in a cobalt-based superalloy fabricated by DED. Scanning electron microscopy (SEM) and transmission electron microscopy (TEM) are used to investigate the spatial distribution and nature of the various phases detected in the as-fabricated microstructure. Energy dispersive X-ray spectrometry (EDS), wavelength dispersive X-ray spectrometry (WDS), and electron energy loss spectroscopy (EELS) are coupled with a fine analysis of the diffraction patterns to identify the different phases decorating the interdendritic regions. These characterizations allow the identification of different submicronic precipitates: Al_2O_3, (Ta,Ti)(N,C), HfO_2, Cr_3B_2 and $(Ti,Zr,Hf)_2SC$. The solidification sequence is discussed at light of the experimental results. This work provides a first understanding of the interplay between solidification segregations and the formation of second phase precipitation in a cobalt-based superalloy processed by DED.

Keywords

γ/γ’ cobalt-based superalloy; Additive manufacturing; Second phase precipitation; TEM

1. Introduction

Additive manufacturing (AM) has shown promising results for rapid prototyping and reparation of superalloys parts in the last decade [1]. However, heritage superalloys from traditional processing routes can exhibit an increased sensitivity to cracking when welded or processed by AM [1,2].

In the solid state, strain-aged cracking can occur due to stress created by the dimensional changes during precipitation of the γ’-phase. In high γ’-phase fraction nickel-based superalloys as in Udimet 720LI, CM247LC or IN939, intergranular solid state cracks are observed following subsolvus temperature holding [2–5]. In the case of cobalt-based superalloys, they exhibit slower γ’-phase precipitation kinetics even with a high γ’-phase volume fraction that causes less hardening at high cooling rates than nickel-based superalloys [6]. This feature is expected to preserve them from strain-age cracking, making them particularly attractive in AM as substitutes for nickel-based superalloys with a high γ’-phase fraction. However, due to their complex chemical

compositions, other cracking mechanisms already known in nickel-based superalloys can occur during AM.

In the liquid state, solidification or liquation cracks in superalloys arise from high cooling rates and high thermal gradients typical of AM processes. These high thermal gradients directly affect the microstructure by promoting the formation of columnar textured microstructures. Combined with the high thermal stresses generated during the process, it results in a synergy leading to a liquid state cracking mechanism. Indeed, during the processing of each layer, solidification microsegregation, and particularly minor elements segregations (boron, zirconium, silicon, hafnium, sulfur, etc.) occur [2,7]. These elements stabilize the residual liquid films during the last stages of solidification and lower the end-of-solidification temperature as is the case for zirconium or boron, see e.g. [8]. Combined with thermal stresses, the presence of a low melting point liquid increases the crack sensitivity of the columnar high-angle grain boundaries in some nickel-based superalloys as in the AD730, IN738LC or IN792 superalloys [2,9–16]. Solidification microsegregation can also lead to the formation of second-phase precipitation such as carbides, borides, eutectic, or Laves phases in the interdendritic regions [17–20]. Due to the multi-layer deposition process inherent to AM, the remelting of these phases can produce liquation cracks in the material that propagate through the layers via high-angle grain boundaries. Moreover, the interdendritic phases can also generate additional stresses, initiate cracks [21–23], or impede liquid flow in the interdendritic regions [24].

To produce crack-free materials, the chemical composition of superalloys has to be adjusted for AM. However, the induced modifications must not affect the hot mechanical properties. Indeed, elements such as boron, or carbon are crucial for mechanical resistance at high temperature and their removal can deteriorate the properties of superalloys [9,25].

To make appropriate chemical changes, it is required to understand solidification microsegregation and the possible formation of second-phase particles during solidification. In addition, their evolution in the solid state during thermal cycling induced by the layer-by-layer nature of the process must be taken into account.

There is now a large body of literature on the additive manufacturing of nickel-based superalloys. For example, Després *et al.* finely characterized the secondary precipitation occurring in nickel-based superalloys processed by laser powder bed fusion (L-PBF) [26] where the cooling rate is very high [1]. On the other hand, only a few studies have been focused on additively manufactured γ/γ’ cobalt-based superalloys [27–30]. To our knowledge, no fabrication by DED has been reported yet. While some similarities between cobalt- and nickel-based superalloys can be expected, some differences are likely to be observed because of differences in affinity between the alloying elements and kinetics of formation of the secondary precipitates [31].

This study aims at characterizing the precipitation and clarifying the solidification path of a γ’-hardened cobalt-based superalloy processed by directed energy deposition (DED). An in-depth characterization is conducted, combining microstructural observations at different scales, chemical analysis, and crystallographic structure recognition. The study focuses on microsegregation and interdendritic phases in order to lay the groundwork for monitoring and controlling their formation sequence, avoiding cracks, and guiding the future chemical design of materials dedicated to AM.

2. Experimental procedures

2.1. Powder characteristics and samples fabrication

In this study, powders of a cobalt-based superalloy were processed as follows: vacuum induction melting (from raw elements), argon atomization, and sieving to collect powder particles ranging from 53 µm to 125 µm. The alloy investigated was already cast and studied by Neumeier *et al.* [32]. CoWAlloy1 exhibits a complex chemical composition with 12 elements. The combination of several alloying elements permits to increase its versatility at high temperature. Chromium, silicon, and boron permits to increase its oxidation behavior at 900°C while γ'- forming elements such as nickel, tantalum, or titanium stabilize the hardening phase at high temperature leading to excellent mechanical properties, especially in creep at 750°C. As for minor elements such as carbon, zirconium, and boron, they contribute to increase the grain boundaries strength. In many aspects, this alloy is better than some commercial nickel-based superalloys [32]. This alloy is considered to be a good candidate to replace nickel-based ones in the next generation of superalloys. Table 1 gives the chemical composition of the as-built material.

Table 1. Nominal composition of the alloy (atomic percent).

	Co	**Ni**	**Al**	**W**	**Ta**	**Ti**	**Cr**	**Hf**	**C**	**B**	**Zr**	**Si**
CoWAlloy1	Bal.	32	6	3	1.5	2.5	12	0.09	0.08	0.08	0.01	0.41

Differential thermal analysis (DTA) experiments were performed to determine the phase transition temperatures using a SETARAM SETSYS Evolution 16/18 under dynamic argon sweep (50 mL/min) with a cooling rate of 10°C/min.

The additive manufactured samples were fabricated using a DED machine LASERTEC 65 DMG MORI equipped with a coaxial nozzle including a 2500 W fiber-guided diode laser with a 3 mm spot size, a 12 g/min powder jet, and a 6 L/min local protective argon shield jet. The 40 × 40 × 10 mm^3 samples were deposited on a 316L stainless steel plate using a bidirectional scanning strategy with a rotation of 90° between each layer (Zig-Zag). DED parameters were kept constant with a laser power of 2000 W, a scanning speed of 900 mm/min. The distance between the nozzle and the manufactured part was set to 0.7 mm. The distance between adjacent molten tracks was set to 1.5 mm. This set of processing parameters was chosen to limit the density of cracks while avoiding lack-of-fusion defects. The relative density of the as-fabricated samples was found to be 99.4%.

Oxygen and nitrogen contents were determined using an ONHG Inductar analyzer on three as-built samples of 120 mg. These contents were measured at respectively 0.01 %at and 0.09 %at.

2.2. Microstructural characterization

The observed samples were extracted from the center of the build-up, far from the substrate. The samples were mechanically polished with a 0.25 µm diamond suspension and a 0.02 µm colloidal silica suspension in a vibratory polisher (Buehler VibroMet 2).

Microstructural investigations were performed using two scanning electron microscopes: a ZEISS MERLIN FEG-SEM, and a TESCAN MIRA3 FEG-SEM equipped with secondary electron (SE) and backscattered electron (BSE) detectors. Energy dispersive spectrometry (EDS) and wavelength dispersive spectrometry (WDS) were conducted in a ZEISS MERLIN FEG-SEM by adapting the high acceleration voltage of

the primary electrons depending on the considered chemical element (SAMx software and SDD detector). EDS was used for the estimation of cobalt, nickel, aluminum, titanium, and chromium while WDS was used to quantify tantalum and tungsten. EDS characterizations were performed on elements that do not have peak interferences. WDS was used for tungsten and tantalum due to their low content and the interferences between Ta(Lα), Ni(Kβ), and W(Lα) peaks. EDS and WDS measurements of each chemical element were preliminary calibrated using pure control samples except for aluminum and titanium where a Ti_3Al complex control sample is used to reduce overlapping peaks.

To isolate small precipitates, site-specific thin foils were lifted out using a HELIOS 660 system integrating SEM and focused ion beam (FIB) technologies. TEM observations of fine precipitates were conducted using a JEOL 2100F TEM at 200kV. EDS, high angle annular dark field (HAADF), and electron energy-loss spectrometry (EELS) were conducted at 200kV using a ZEISS LIBRA 200 TEM. EDS enabled the identification of almost all solutes present in the alloy composition and EELS completed the measurements with more sensitive detection of light elements such as carbon, boron, or nitrogen. While the Kα line was used in EDS for oxygen, nitrogen, carbon, sulfur, aluminum, titanium, and chromium identification, the Mα line was used for hafnium because of the interfering signal from the copper Kα and Kβ lines coming from the sample holder. The Lα line was used for the tantalum identification. The chemical identification allowed us to make assumptions regarding the most likely precipitating phases (Table 2).

To recognize the crystallographic structures of the low volume fraction phases, automated crystal orientation mapping (ACOM) was acquired with a 5 nm step size using the ASTAR™ hardware and software toolset provided by NanoMegas [33,34]. ASTAR™ computes diffraction patterns of the candidate phases implemented in the software resulting from the chemical identification (Table 2). Then, the simulated diffraction patterns of the candidate phases are compared with those acquired on the JEOL TEM at each pixel of the region of interest. During the acquisition of the diffraction patterns, a precession angle of 1.2° was applied [34]. The correlation of experimental and simulated patterns is evaluated by an index I that is sensitive to the spots size and their intensity. The correlation index permits to compute the phase reliability index R of each candidate phase, $R=100*(1-I_1-I_2)$ with I_1 and I_2 the correlation indexes of the two best solutions for the phase recognition. A phase reliability R higher than 15 is usually considered as sufficient to ascertain that the recognized phase is by far the solution out of all phases implemented in the database [34].

Coupling in-depth chemical analysis with crystallographic structure recognition of a zone is a good way to ascertain the presence of some phases.

Table 2. Candidate phases implemented for the ACOM analysis.

Phase	Space group	Lattice parameters (Å)	Lattice angles (°)	Reference
Matrix (γ/γ')	Fm$\bar{3}$m (225)	3.57, -, -	90, -, -	[35]
TaC	Fm$\bar{3}$m (225)	4.45, -, -	90, -, -	[36]
TiN	Fm$\bar{3}$m (225)	4.24, -, -	90, -, -	[37]
Al_2O_3 (Tetragonal, δ)	P$\bar{4}$m2 (115)	5.59, -, 23,66	90, -, -	[38]
Al_2O_3 (Monoclinic, θ)	C2/m (12)	11.79, 2.91, 5.62	90, 103.79, 90	[39]
HfO_2 (Monoclinic)	$P2_1/c$ (14)	5.12, 5.19, 5.29	90, 99.35, 90	[40]
HfO_2 (Orthorhombic)	Pbca (61)	10.02, 5.23, 5.06	90, -, -	[41]
HfO_2 (Orthorhombic)	Pbcm (57)	5.01, 5.23, 5.06	90, -, -	[42]
Cr_2O_3	R$\bar{3}$C (167)	5.35, -, - 4.96, 4.96, 13.59	55, -, - 90, -, 120	[43] [44]
TiO_2	$I4_1/amd$ (141) Pbca (61)	3.73, -, 9.37 9.17, 5.45, 5.14	90, -, - 90, -, -	[45] [46]
TiS	$P6_3/mmc$ (194)	3.30, -, 6.38	90, -, 120	[47]
Ti_2SC	$P6_3/mmc$ (194)	3.21, -, 11.20	90, -, 120	[48]
Cr_5B_3	I4/mcm (140)	5.46, -, 10.64	90, -, -	[49]
Cr_3B_2	P4/mbm (127)	5.79, -, 3.06	90, -, -	[50]

3. Experimental results

3.1. Microstructural overview

The cobalt-based superalloy exhibits typical features of microstructures [51] inherited from the DED process with large columnar grains growing along the building direction (Figure 1 (a)). This columnar grain structure results from epitaxial growth from the underlying layers. A dendritic microstructure is observed with the primary trunks aligned with the building direction (Figure 1 (b)). Images were taken using the BSE contrast in the interdendritic regions and revealed the presence of microsegregation of heavy elements.

The primary dendrite arm spacing (PDAS, λ_1) was measured using the intercept method along the height of the sample. The PDAS was found to be constant along the height from 2 mm up to the top region and was measured to be roughly equal to 13.3 ± 1 µm. Zhang *et al*. established the following formula, $\lambda_1 = 134.43(\dot{T})^{-0.26}$, on a nickel-based superalloy to estimate the cooling rate ($\dot{T}$) [52]. This empirical law is relatively insensitive to the chemical composition for nickel-based alloys [52]. Given that the thermal properties of cobalt-based superalloys are relatively close to that of the nickel-based ones [53], the above-mentioned law permits to assess the process cooling rate. The estimated cooling rate, $\dot{T} = 7 \times 10^3 \pm 2 \times 10^3$ K/s in the studied alloy, is in agreement with the typical cooling rates encountered in DED [1].

As-built samples contain a high density of intergranular cracks propagating along high-angle grain boundaries as found in additively manufactured nickel-based superalloys, see e.g. [11,54,55] or aluminum alloys [56]. Over the intergranular cracks observed in this work, no crack was found propagating along grain boundaries with a misorientation smaller than 20°. A dendritic morphology was observed at the crack surface, see e.g. Figure 1 (c).

Large γ/γ' eutectic phases and multiphase interdendritic precipitates were detected in the interdendritic regions. These phases were characterized, from 2 mm above the

substrate to the top of the sample (about 12 mm), decorating the grain boundaries or the interdendritic regions as well as in the vicinity of cracks as illustrated by Figure 1 (d). XRD measurements (see Supplementary figure 1) only reveal the presence of the γ-matrix hardened by the γ'-precipitation. The low volume fraction of the interdendritic phases does not allow their detection by XRD. As a result, their identification requires further characterization using more local and advanced characterization techniques.

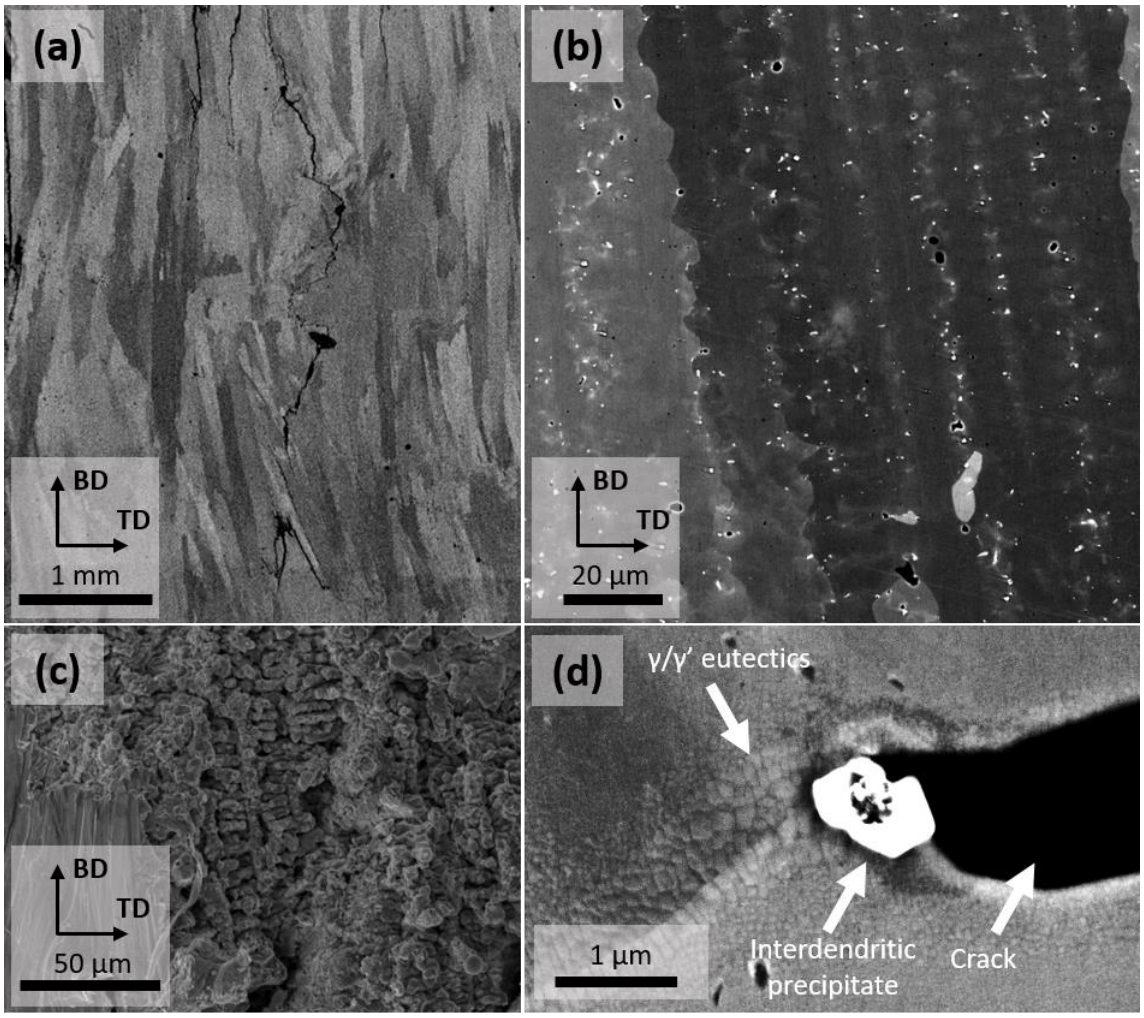

Figure 1. (a) As-built microstructure in the center of the sample (BSE). BD is the building direction and TD is the transverse direction. (b) Dendritic microstructure near a grain boundary (BSE). (c) Crack surface exhibiting a dendritic morphology (SE). (d) Interdendritic precipitates located near a crack tip (BSE). (2-column fitting image)

3.2. Complex multiphase interdendritic precipitation

In the present study, interdendritic precipitates are observed mostly in the interdendritic regions or along the grain boundaries as revealed by the bright contrast of the particles when using the BSE detector. These precipitates appear to be aligned with the direction of dendrite growth (particles with a bright contrast in Figure 1 (b)). EDS and WDS analyses show the solidification microsegregation of elements across the interdendritic regions (Figure 2). The γ-forming elements, such as cobalt and chromium, segregate in the dendritic core, whereas the γ'-forming elements, such as nickel,

aluminum, tantalum, and titanium, segregate in the interdendritic regions. Among the γ'-forming element, only tungsten segregates in the dendritic core, which is consistent with previous observations in cobalt-based superalloys [57–62]. It can be noticed that microsegregation inherited from solidification is still observed despite the solid state thermal cycling of the DED process. Indeed, the observed area in Figure 2(b) is at the center of a 40 × 40 × 10 mm^3 build-up and thus has been potentially thermally affected by the deposition of multiple layers.

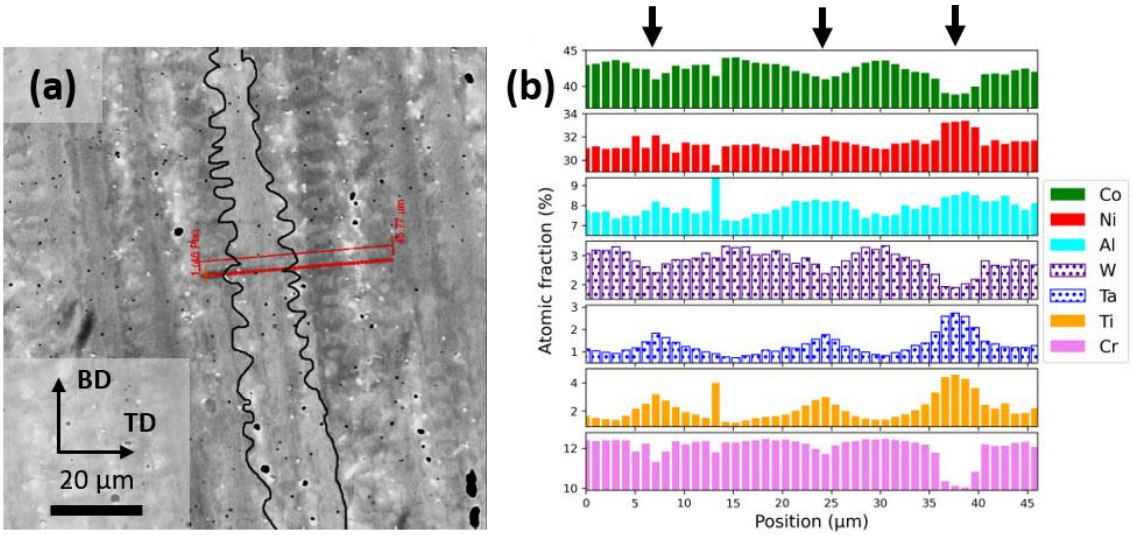

Figure 2. (a) EDS and WDS profiles orthogonal to the dendritic growth axis crossing several dendrites. (b) Segregations of major elements along the profiles measured by EDS (filled bar) and WDS (dotted bar), the black arrows indicate the interdendritic areas. (Color figure, 2-column fitting image)

The progressive enrichment of the liquid in γ'-forming elements (Figure 2) seems to be correlated with the gradient of γ'-size. Similar segregation profiles and precipitation have been observed in nickel-based superalloys [18]. Figure 3 shows the γ'-size gradient between two interdendritic regions in the center of an as-built sample.

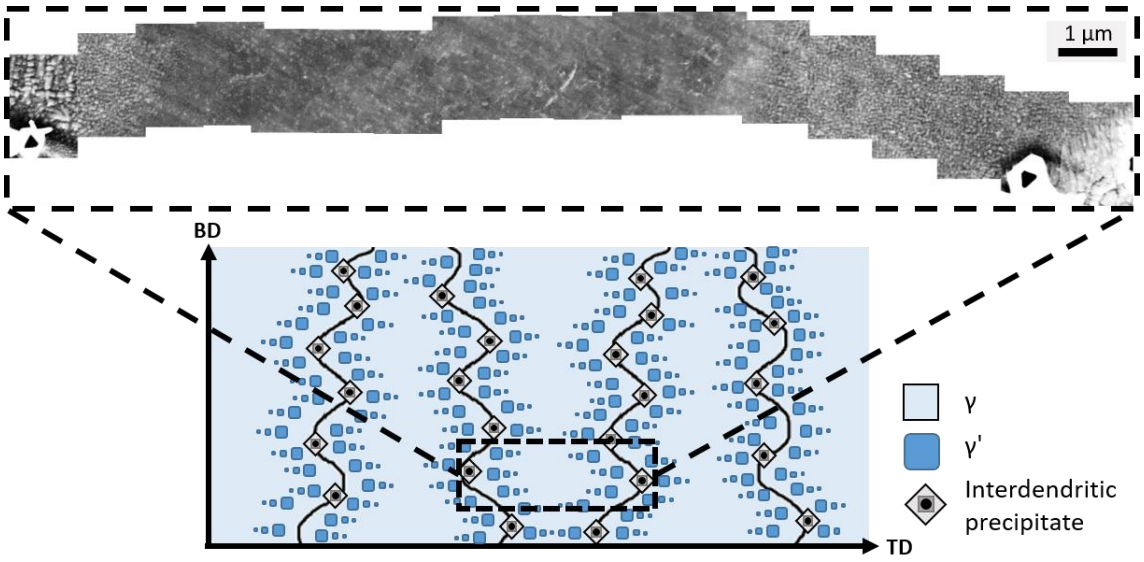

Figure 3. Illustration of the γ'-size gradient between two interdendritic regions in the as-built conditions. (Color figure, 2-column fitting image)

Several types of precipitates, with peculiar morphologies and arrangements, can be found in the interdendritic regions, as illustrated in Figure 4. A first type is made of a core consisting of spherical particles (Figure 4 (d)) around which a more facetted shell can be seen (Figure 4 (b)). This shell progressively evolves from dark contrast inside to light contrast when observed by HAADF (Figure 4 (b) and (c)). This suggests a progressive evolution of the shell chemical composition. Besides the core-shell type of precipitate, other types of precipitates are detected using HAADF, see red, blue, and yellow arrows in Figure 4 (a).

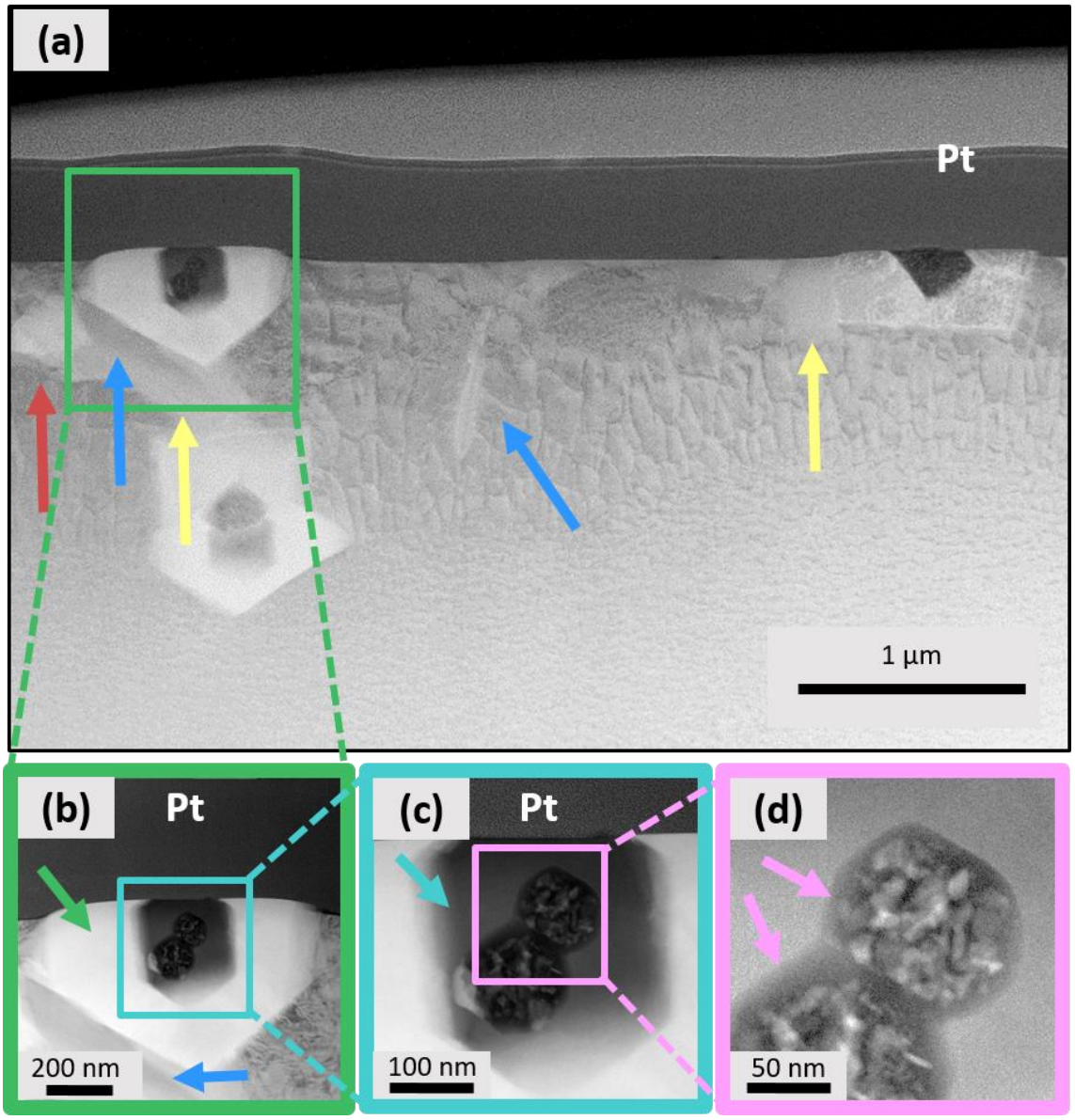

Figure 4. (a) Interdendritic precipitates observed by TEM (HAADF). Red, blue, and yellow arrows indicate isolated type 1, 2 and 3 precipitates respectively. (b) Enlarged view of the external shell of a multiphase interdendritic precipitate. (c) Enlarged view of the internal shell of a multiphase interdendritic precipitate. (d) Enlarged view of the core of a multiphase interdendritic precipitate. The upper layer in (a), (b), and (c) corresponds to the platinum layer deposited during FIB operation to protect the surface. (Color figure, 2-column fitting image)

3.2.1. Precipitate core

The spherical particles inside the internal shell (Figure 4 (d)) exhibit local compositional variations as highlighted by the chemical contrast of the HAADF images shown in Figure 4 (d) and Figure 5 (a). Elemental mapping of these precipitates was carried out by EDS (Figure 5 (a)) to estimate solute enrichments in such particles. It appears that the core-phase is enriched in aluminum, hafnium, and oxygen. The alumina (Al_2O_3 (tetragonal, δ)) and hafnia (HfO_2 (orthorhombic, *Pbca*)) phases are recognized during ACOM mapping as shown by the diffraction patterns displayed in Figure 5 (b). Those particles are relatively small, about 100 nm. Diffraction patterns are a bit noisy

due to the combination of both alumina and hafnia patterns. It is particularly the case in the hafnia diffraction patterns due to their small size in the nutshell core. The superposition of the alumina and the hafnia diffraction spots leads to rather low phase reliability for the hafnia (R=6). However, the above-mentioned phases display the best correlation with ASTAR™ among the candidate phases (Table 2).

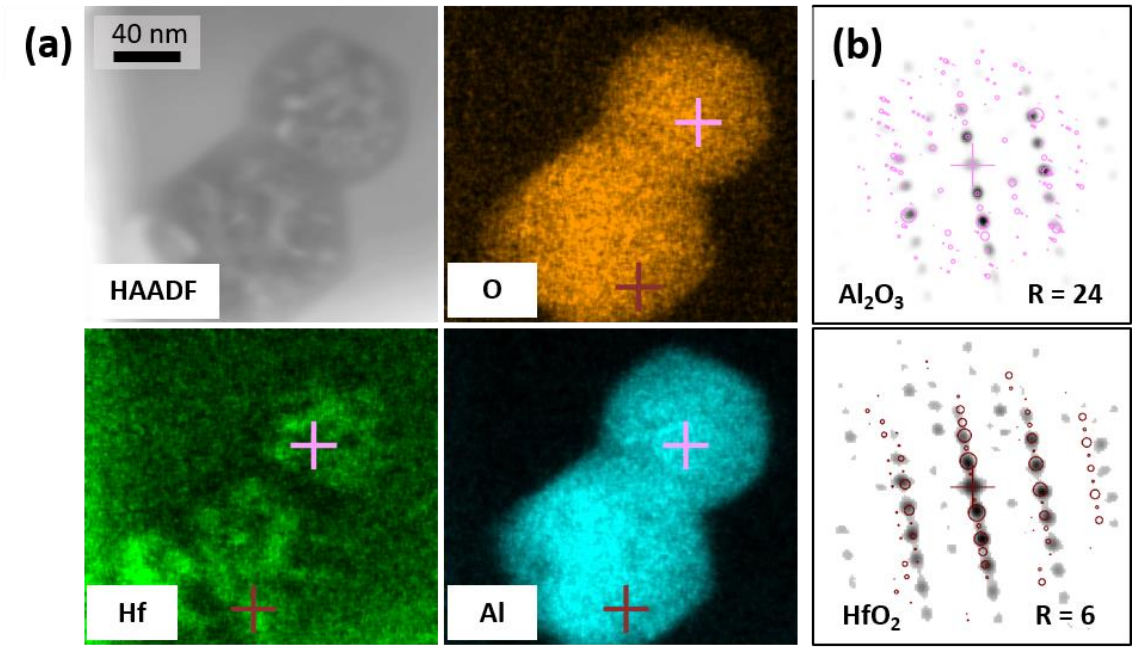

Figure 5. (a) HAADF and elemental maps of alumina and hafnia. (b) Experimental diffraction patterns compared to the simulated patterns (in circled) of the areas marked with a cross. (Color figure, 2-column fitting image)

3.2.2. Precipitate shell

The facetted shell of the precipitates consists of a 1 µm width external shell (Figure 4 (b)) and a 300 nm width internal shell (Figure 4 (c)). The HAADF map and the EDS measurements clearly reveal the chemical composition evolution of the shell (Figure 6 (a)). Titanium and nitrogen are the main elements in the internal shell, and tantalum and carbon progressively substitute these two elements in the external shell (Figure 6 (a)). The lattice parameters of the TiN and TiC phases are very close, which induces almost no difference in the ACOM simulated pattern. For this reason, we decided to implement only TiN in the ACOM. The resulting mapping of the ACOM analysis matches very well with TiN for the internal shell and TaC for the external shell (Figure 6 (b)) confirming a progressive increase of the lattice parameter from the one of TiN, 4.24 Å to that of TaC, 4.45 Å. The crosses shown in Figure 6 (a) and their associated diffraction patterns in Figure 6 (b) illustrate the two extreme limits of this progressive evolution. Several studies presented the chemical evolution from nitride core to carbide shell [26,63]. Despite the difference between the two lattice parameters being rather small, this is well captured by ACOM.

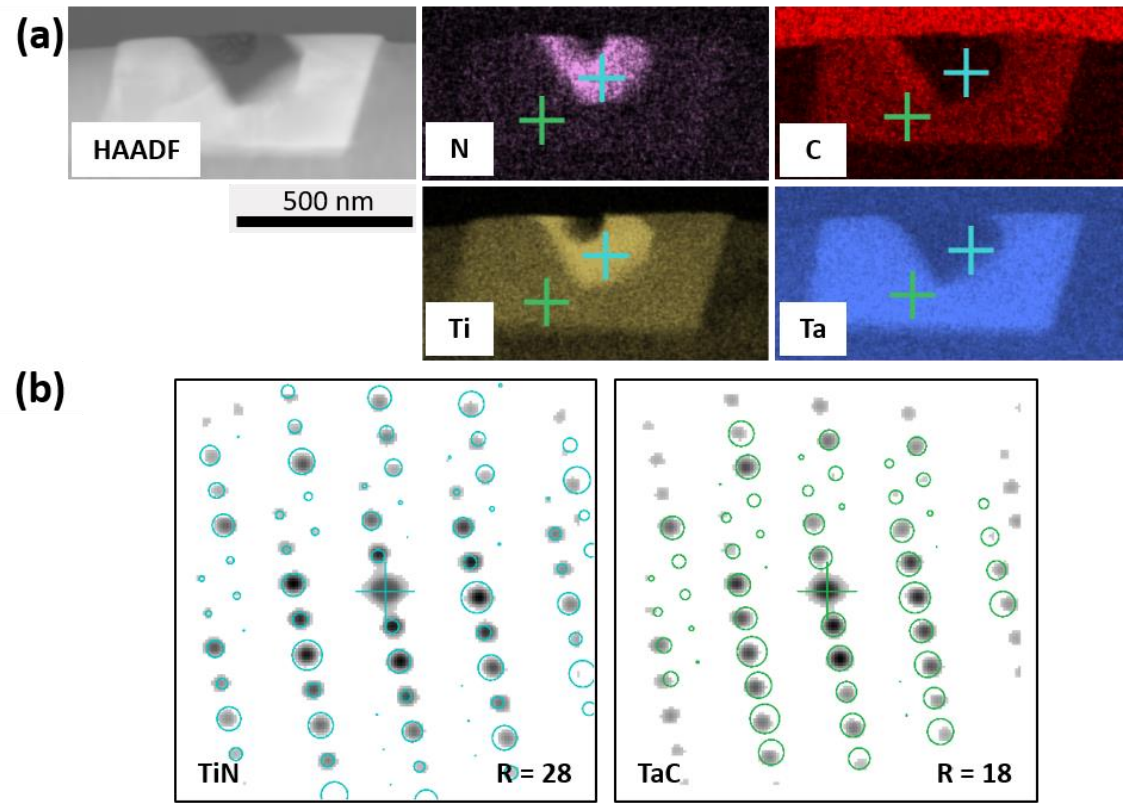

Figure 6. (a) HAADF and elemental maps acquired by EDS of a carbonitride. (b) Experimental diffraction patterns compared to the simulated patterns (in circled) of the areas marked with a cross. (Color figure, 2-column fitting image)

EELS analyses of nitrogen and carbon provide chemical information to complete the crystallographic information deduced from the ACOM analysis. The EELS results confirm the presence of nitrogen associated with titanium corresponding to the TiN phase. The platinum deposited during the FIB process reduces the carbon signal. However, the EDS enrichment mapping clearly reveals the carbon enrichment in the particle identified as a carbide (Figure 6 (a)).

Finally, these phases are qualified as carbonitrides composed of titanium and tantalum ((Ti,Ta)(N,C)). The particles are identified as TiN that progressively becomes TaC. The transition from TiN to TaC is smooth due to their crystallographic similarities (same space group and close lattice parameter).

3.2.3. Isolated precipitates

In the interdendritic region, several isolated phases with different morphologies are observed, see arrows pointing out isolated precipitates in Figure 4 (a).

EDS measurements reveal enrichment of hafnium and oxygen in a particle with a rounded shape (see the red arrow pointing to the isolated precipitate in Figure 4 (a) and Figure 7 (a)). These elemental maps suggest the presence of hafnia, which is confirmed by the ACOM recognition (HfO_2 (monoclinic) in Figure 7 (b)).

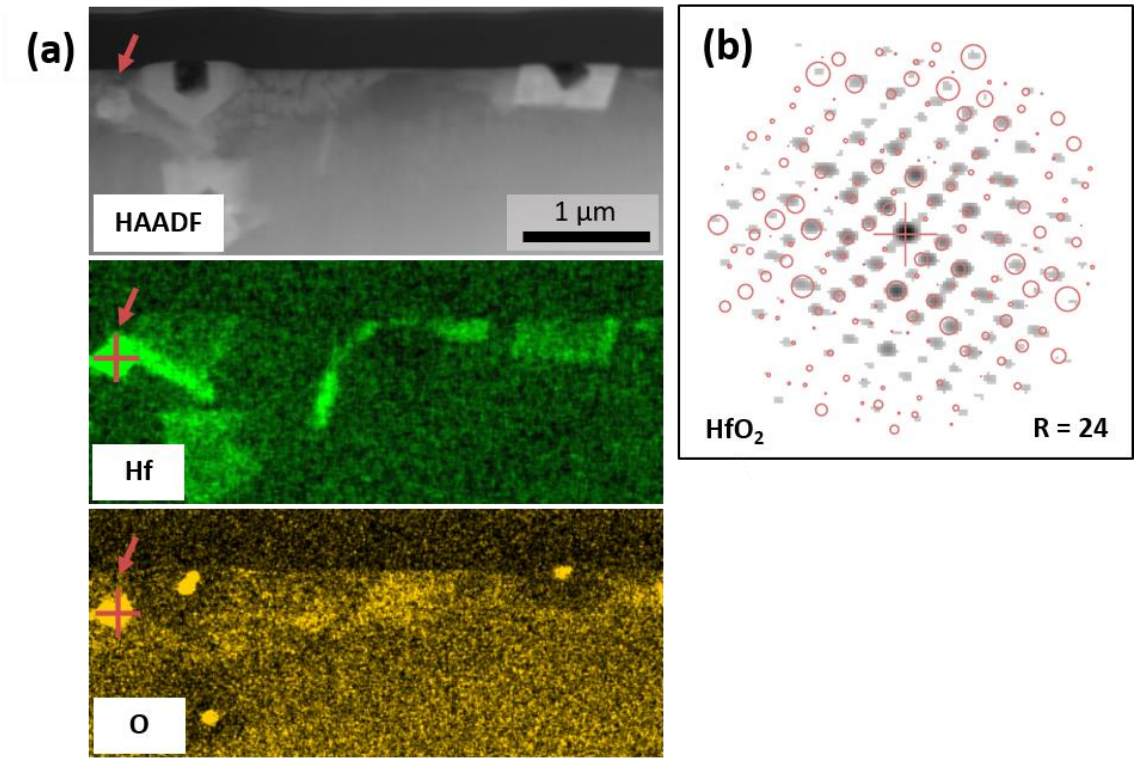

Figure 7. (a) HAADF and elemental maps acquired by EDS of an hafnia particle (indicated by the red arrow). (b) Experimental diffraction pattern compared to the simulated pattern (in circled) of the area marked with a cross. (Color figure, 2-column fitting image)

Another kind of isolated precipitate is observed with a characteristic needle shape of 1 µm in length, see the blue arrow pointing to the isolated type 2 precipitate in Figure 4 (a)). These precipitates appear to be rich in carbon, sulfur, and titanium (Figure 8 (b)). These precipitates also contain some zirconium and hafnium, which seem to substitute titanium. A good correlation is obtained using ACOM for $(Ti,Zr,Hf)_2SC$ sulfocarbides (Figure 8 (c)).

Contrary to Sanviemvongsk *et al.* who did not identify the crystallographic structure of carbon and sulfur enriched particles and only assumed their presence due to the small size of precipitates from L-PBF [64], the recognition of the crystallographic structure of sulfocarbides by ACOM is excellent (Figure 8 (c)).

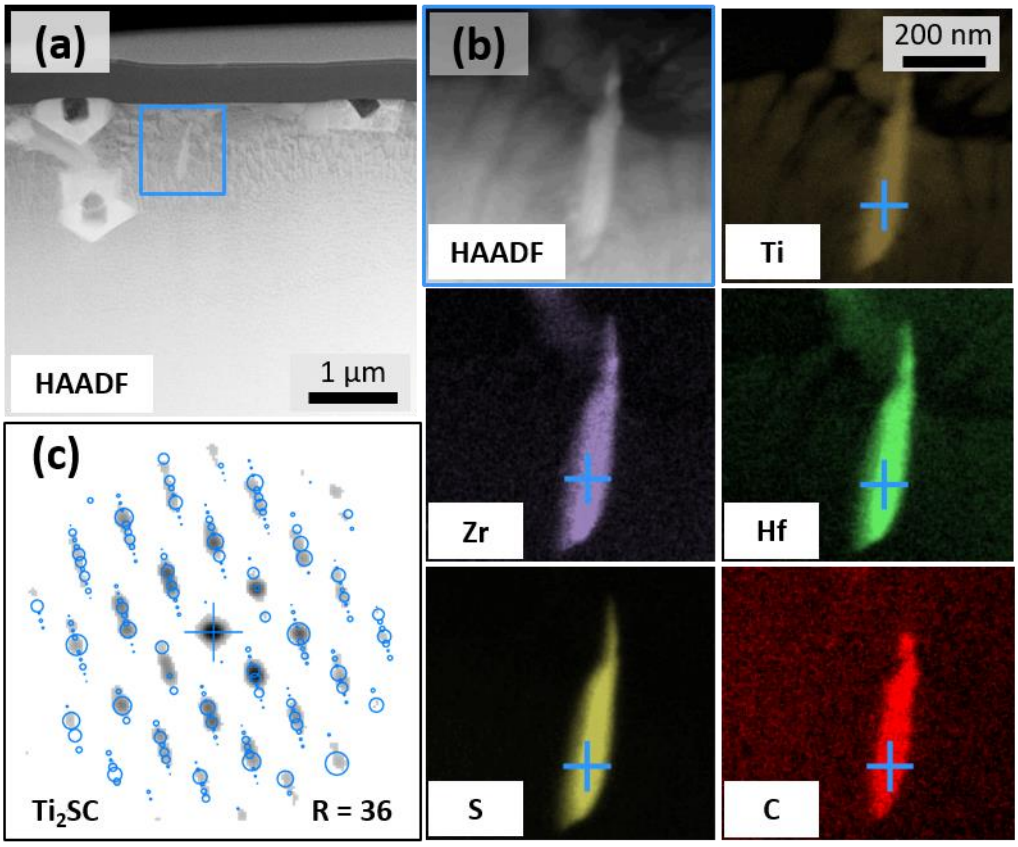

Figure 8. (a) HAADF and elemental maps acquired by EDS of sulfocarbide. (b) Experimental diffraction pattern compared to the simulated pattern (in circled) of the area marked with a cross. (c) Region of interest analyzed in the site-specific lift-out. (Color figure, 2-column fitting image)

In the interdendritic area, isolated type 3 precipitate with an elongated and spherical shape remains unidentified (Figure 4 (a), yellow arrows). One of these precipitates is in contact with a sulfocarbide as shown in Figure 9. EDS measurements reveal a chromium enrichment in these precipitates. ACOM analysis reveals the best correlation with the Cr_3B_2 structure in the phases implemented (Table 2). However, the diffraction pattern recognition is not enough relevant to confirm the boride structure. In order to eventually detect the presence of boron in such precipitates, EELS measurements were conducted. However, no boron has been found, probably due to the thickness of the site-specific thin foils where borides are located which alleviates the B signal.

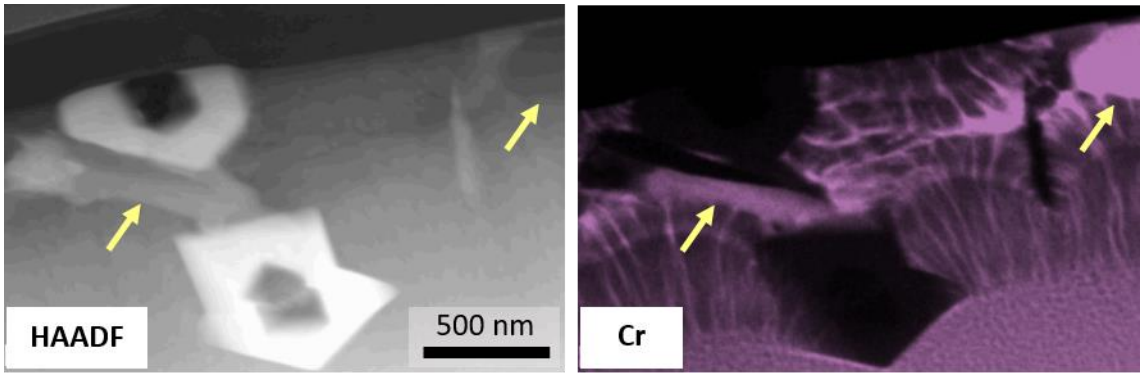

Figure 9. HAADF and Cr elemental map acquired by EDS of precipitates suspected to be borides (indicated by yellow arrows). (Color figure, 2-column fitting image)

3.2.4. Complex multiphase precipitate

Figure 10 summarizes the identification of the precipitating phases in the interdendritic areas. In the ACOM maps (Figure 10), it can be noticed that areas with low phase reliability (dark contrast on Index recognition map, Figure 10) are recognized as alumina or hafnia. Indeed, the ACOM method always recognizes a phase in the implemented ones and the complex crystallographic structures of alumina and hafnia often show the best correlation with poor quality diffraction patterns as can be the case for instance with the needle of alumina near the sulfocarbide. The non-relevancy of the ACOM recognition in some areas is likely due to the large thickness of the site-specific lift-out or due to overlapping diffraction patterns at the boundaries between the different phases. As discussed above, it can also be noticed that the pattern identification of the boride crystallographic structure is not enough relevant to isolate a single boride phase.

The chemical measurements and crystallographic recognition coupling permit an almost complete identification of the complex multiphase precipitates observed in the as-built microstructure. This characterization highlights the efficiency of this approach for complex microstructures such as those inherited from AM [26,65].

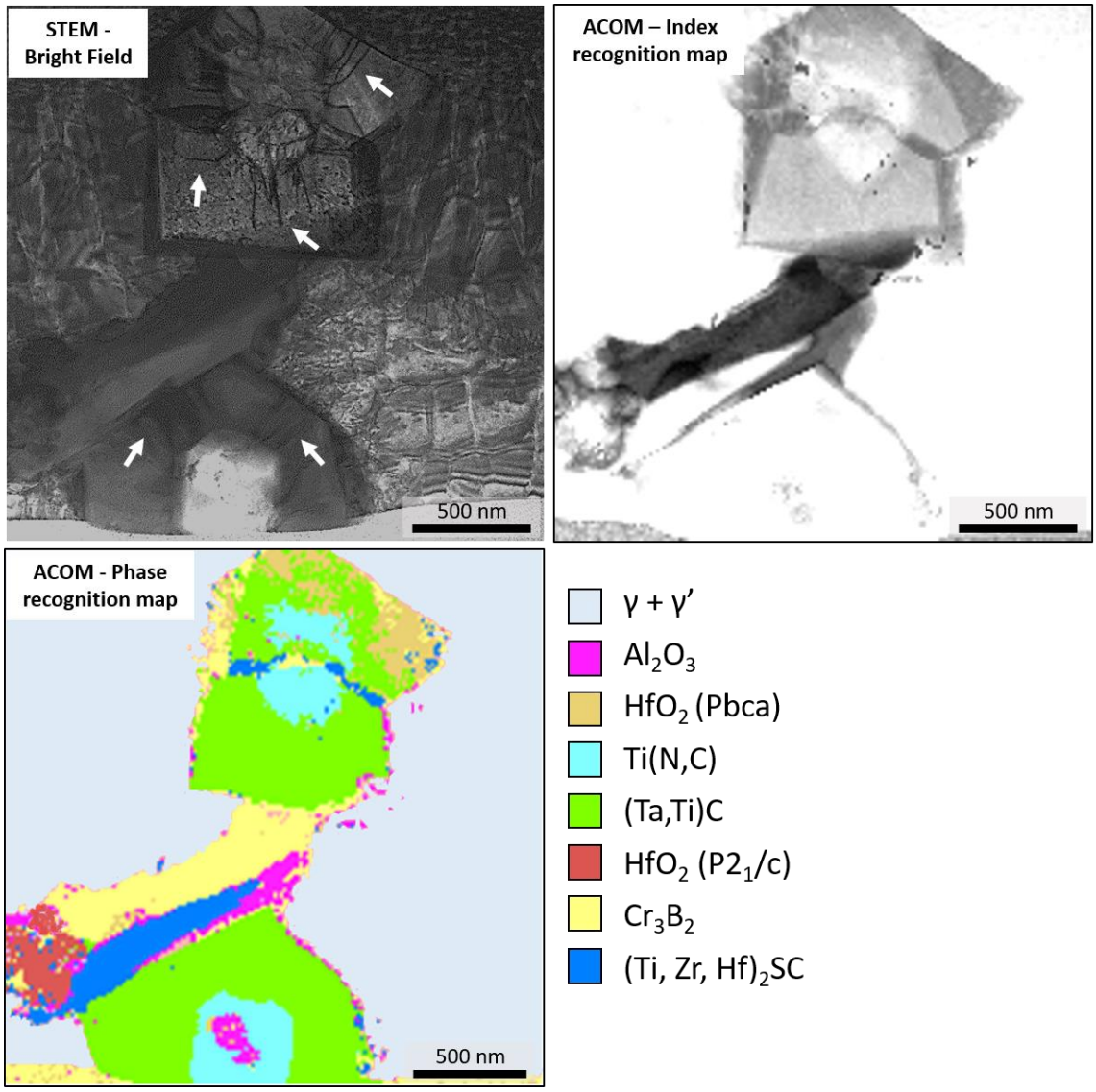

Figure 10. Recognition of the different interdendritic phases precipitating during directed energy deposition. The index recognition map evaluated the reliability of the phase recognition. The darker the contrast the lower the phase identification reliability. The white arrows on the STEM bright field highlight the presence of dislocations inside the carbides. (Color figure, 2-column fitting image)

4. Discussion

The additive manufacturing of CoWAlloy1 by DED leads to the appearance of numerous intergranular cracks. The dendritic morphology of the observed fracture surfaces is the signature of cracking in presence of liquid films (see Figure 1 (c) and refs. [11,16,66]). Several studies made on nickel-based superalloys attribute the genesis of this cracking mechanism to the solidification microsegregation and the precipitation of second phases in the interdendritic regions. In our study, all interdendritic phases have been identified as a result of the experimental observations coupling crystallographic information with chemical analyses. The interdendritic particles nucleate due to the microsegregation and the specific solidification path during AM. For the first time, this complex multiphase precipitation is finely analyzed in the CoWAlloy1. The origins and the peculiarities of segregations in the cobalt-based superalloys are discussed as well as the precipitation order of the different phases.

4.1. Solidification microsegregation

During direct energy deposition of the CoWAlloy1, solidification microsegregation occurs. With the progress of solidification, the liquid is progressively depleted in cobalt, tungsten, and chromium. These elements partition mainly in the dendrite cores to form the γ-matrix (Figure 2 (b)). As solidification proceeds, aluminum, tantalum, and titanium segregate into the liquid. These elements are thus found in the interdendritic spaces (Figure 2 (b)).

As illustrated in Figure 3, the microsegregation measured by EDS/WDS (Figure 2) directly affects the γ'-precipitate size. The γ'-size differences between cores and boundaries of dendrites are explained by the microsegregation in aluminum, tantalum, and titanium (γ'-forming elements) and the depletion in tungsten and γ-forming elements in the liquid during solidification. The enrichment of γ'-forming elements such as tantalum or titanium in the interdendritic areas leads to an increase in the γ'-solvus temperature and makes more stable this phase. In contrast, dendritic cores are enriched in γ-forming elements such as chromium that inhibit the formation of the γ'-phase [67]. Furthermore, enrichment in tungsten in the dendritic cores (γ'-forming element) slows down the chemical diffusion, and therefore the growth and coarsening of the γ'-precipitates. The higher solvus temperature in the interdendritic areas leads to the precipitation of the γ'-phase at a higher temperature, during the last stages of solidification, compared to the dendritic cores explaining the γ'-precipitate size gradient (Figure 3). Although only segregations of major elements (> 1%at) are measured, minor elements (< 1 %at) have been reported to also segregate in the interdendritic areas and grain boundaries [2,11,13,17]. The γ'-size gradient is also thought to be due to the microsegregation in hafnium and zirconium in the residual liquid. Indeed, these elements stabilize the γ'-phase and promote the formation of coarse precipitates and γ-γ' eutectics [7,68].

4.2. Solidification precipitation

During solidification and due to both segregations of major and minor elements, solubility limits of several elements can be exceeded promoting the formation of interdendritic precipitates. Some phases can nucleate during solidification and their chemical compositions can evolve with the solidification segregations in the liquid. The sequence of precipitation of the various observed phases during solidification is now discussed.

The spherical particles of alumina seem to be the first particles present in the liquid at high temperatures as shown by their position at the core of core-shell precipitates (Figure 4 and Figure 10). The alumina melting point is around 2050°C [69], i.e. upper than the liquidus of the alloy investigated, which has been measured at around 1411°C by DTA. There are two hypotheses on the origin of the alumina particles. Whether the alumina cores are the first phases that nucleate in the liquid or they come from undissolved oxides. These undissolved phases can form during the powder elaboration or either from oxygen captured during DED that precipitates during solidification [70]. In any case, these alumina particles are present first in the liquid, above 1600°C. This core-shell structure with alumina at the core has never been observed in DED parts, but it has been frequently observed in plasma cladding [71] or in L-PBF parts made of the AD730 superalloy [26] and 2024 aluminum alloy [72]. The main difference with core-shell in L-PBF parts is the size of the precipitates, which is larger in DED parts owing to slower

cooling rates. As a result, one can see the particles in the DED microstructure as an enlarged view of those observed in L-PBF microstructures.

Then, carbonitrides start nucleating onto the spherical particles of alumina. The solubility limit of nitrogen at 1600°C in nickel-based superalloys is around the measured content in the as-built alloy. Indeed, 900ppm of nitrogen are measured in the CoWAlloy1 and the nitrogen solubility limit is about 10ppm in pure nickel, 100ppm in Ni-8Cr, and reaches nearly 1000ppm in Ni-24Cr [7]. It seems thus that TiN nucleate before the γ-matrix solidification, just below 1600°C, when TiN becomes more stable than TiC (see the Ellingham diagram given in Supplementary figure 2). During the thermal cooling and the depletion of nitrogen in the liquid, these titanium nitrides progressively evolve from TiN to Ti(N,C). The formation of MC carbides above the eutectic temperature is promoted by the presence of TiN nuclei [73]. This transition happens when nitrogen is almost totally consumed in the liquid around 1300°C, below the liquidus temperature of the γ-matrix. After this transition from TiN to TiC, carbides keep evolving above the solidus temperature to (Ta,Ti)C and finally TaC. The substitution of titanium for tantalum can be explained by the higher stability of TaC compared to TiC [2,7,74] as shown by the Ellingham diagram provided as Supplementary figure 3. The lattice parameter, mentioned in Table 2, slowly increases from TiN to TaC with the progressive chemical evolutions. Several similar observations have been made in nickel-based superalloys made by more conventional processing routes [7] and AM [26]. It must be mentioned that the precipitation of carbonitrides seems to be dissociated from the γ-matrix solidification. Indeed, no orientation relationships between carbides and the γ-matrix were found in this work. These particles seem to heterogeneously precipitate around the alumina core in the liquid at high temperature and are pushed towards the interdendritic regions when the solid-liquid interface advances.

At lower temperatures, during solidification, other phases precipitate due to microsegregation in the liquid. First, the γ'-phase precipitates as discussed above and then, during later stages, other second phases. Borides and sulfocarbides are observed at the tip of the dendrite arms. Their formations are mentioned in other studies due to boron and sulfur segregations in the interdendritic areas at the very end of solidification near the solidus of the γ-matrix [2,7,20,26]. Borides nucleate due to a large enrichment of boron that reaches the solubility limit of this element in the matrix [11,26]. As for the needle-like sulfocarbide, titanium, zirconium, and hafnium have a high affinity with sulfur (it can be noticed that these elements belong to the same column of the Mendeleïev table) [7,75]. These three elements segregate in the interdendritic areas during solidification and precipitate as sulfocarbides in the last liquid [7,75] (Supplementary figure 2). De Luca *et al.* already observed titanium sulfides at the cell boundaries in a carbon-free nickel-based superalloy elaborated by L-PBF [10]. These sulfides are supposed to neutralize sulfur embrittlement at grain boundaries by consuming sulfur present in solid solution [7,75].

After the precipitation of borides and sulfocarbides, the alloy is fully solidified [7,75,76]. At this stage, the interdendritic areas consist of borides, sulfocarbides, carbonitrides around the alumina core but also free alumina round precipitates around which no carbonitride has nucleated.

4.3. Microstructural evolutions during the intrinsic heat treatment

Once the solidification is completed, the thermal cycling in the solid state keeps continuing due to the multi-layered process of DED playing the role of an in situ

anisothermal heat treatment. The latter is sometimes described as an “intrinsic heat treatment” in the literature [77,78]. During the elaboration of the first upper layers, some phases can be remelted or dissolved such as the borides, sulfocarbides, or the γ-γ’-eutectic [2,7]. Then, during the elaboration of the next layers, microstructural evolutions in the solid state can occur. Thus, the solidified microstructure and the size, composition, and morphology of the various precipitates can keep evolving.

The presence of hafnia particles on the spherical alumina core (Figure 5) can be explained by the reduction of alumina by hafnium in the solid state during the intrinsic heat treatment during DED via the following reaction: $\frac{2}{3}Al_2O_3 + Hf \rightarrow \frac{4}{3}Al + HfO_2$. Hafnium is present in the carbonitrides around the alumina core (Hf elemental map in Figure 7 (a)). Due to the intrinsic heat treatment during DED, hafnium can migrate from the carbonitride shell to the alumina core and partially reduce the already formed alumina into more stable hafnium oxides (see Supplementary figure 4). A parallel can be drawn with the study of Després *et al.*, where the transformation of alumina into zirconia (ZrO_2) has been observed in L-PBF in the presence of zirconium, an element that belongs to the same column as hafnium in the Mendeleïev table [79].

The presence of hafnia in the interdendritic area can also be the result of the reduction of other oxides. Indeed, it should be noticed that the interdendritic areas are also rich in aluminum (Figure 2 (b)) that could come from former free particles of alumina. During the intrinsic heat treatment, this population of free alumina round particles can be totally reduced by the hafnium present in solid solution in the interdendritic areas or segregated at grain boundaries to form hafnia. Hafnia is more stable than alumina in the DED process temperature range (see Supplementary figure 4). This reduction can explain why no isolated particle of alumina is observed at the dendritic tips. Moreover, the total reduction of alumina by hafnium can explain crystallographic structure changes. Indeed, ACOM recognizes orthorhombic hafnia in the alumina core (Figure 7 (b)) and monoclinic hafnia in the isolated precipitate where no alumina is found (Figure 5 (b)). After the total reduction of alumina, the orthorhombic hafnia can be free to decompose in its more stable monoclinic structure [80,81].

Due to the thermal cycling, the solid state evolution of other phases cannot be excluded. Borides and sulfides are found in the non-liquated interdendritic areas near carbonitrides (Figure 4). However, they are no longer observed in the vicinity of liquation cracks with the carbonitrides (Figure 1 (d)). Due to the multi-layered process, remelting of these phases is possible and would release boron and sulfur in the residual liquid. Such a mechanism can contribute to increase the sensitivity of the alloys to liquation cracking [2,7,20]. As for the carbonitrides, several indications suggest that these phases result mainly from solidification and not from solid state phase transformations during the intrinsic heat treatment. For instance, carbonitrides are still observed in the crack vicinity (Figure 1 (d)) even if there are likely to decompose in $M_{23}C_6$ during the intrinsic heat treatment via the following transformation: $MC + \gamma \rightarrow M_{23}C_6 + \gamma$ [2,7].

4.4. Summary of the microstructural evolution

Chemical and crystallographic characterizations are complementary and enable to establish the solidification path of the CoWAlloy1 elaborated by DED. This qualitative result is summarized in Figure 11 where the evolution along the Z-direction is consistent with the evolution of the temperature seen by the alloy.

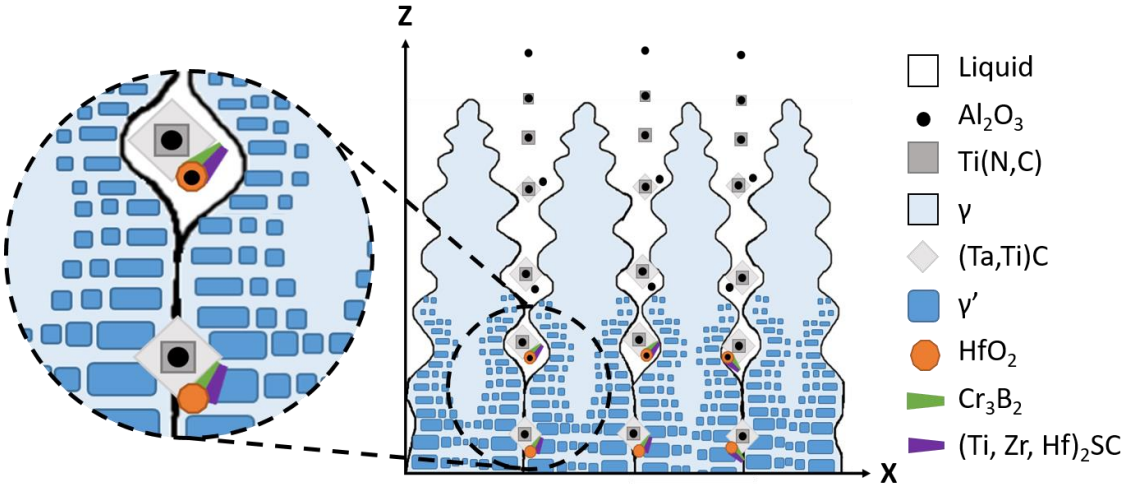

Figure 11. Summary of the solidification path of the cobalt-based superalloy CoWAlloy1. (Color figure, graphical abstract, 2-column fitting image)

Contamination by the atmosphere or the presence of pre-existing oxides on the powder surface leads to residual contents of oxygen and nitrogen in the molten alloy during its directed energy deposition. The aluminum oxides resulting from these phenomena agglomerate as spherical particles that act as heterogeneous nucleation sites for other phases. Then, during gradual solidification, the liquid saturates in nitrogen promoting the formation of titanium nitrides around the spherical oxides. The nitrides progressively evolve into carbonitrides and then into carbides when the saturation point of carbon is reached in the liquid. The chemical composition of the carbide changes from TiC to TaC. The precipitation sequence continues with the formation of chromium borides and titanium sulfocarbides near the tantalum carbides. At low temperatures, at the end of the solidification or in the solid state due to the intrinsic heat treatment during DED, hafnium partially or completely reduces alumina to form hafnia. The last formed particles such as borides, sulfides or hafnia appear to be detrimental to the material crack sensitivity. During the multi-layered deposition process, they can remelt and promote the formation of a liquid film at grain boundaries, which can induce cracks.

5. Summary and conclusion

This paper presented the solidification path of a γ/γ' cobalt-based superalloy, through a careful and detailed microscopic characterization. The following outcomes were obtained.

(1) Chemical analyses and automated crystal orientation mapping enable the establishment of the complete solidification path of cobalt-based superalloys elaborated by DED. All the phases observed in the as-built interdendritic areas are identified.

(2) The formation of complex multiphase precipitates in the interdendritic areas is driven by the segregation of minor elements in the last liquid. Alumina oxide plays the role of germination site around which carbonitride grows. At the end of solidification, phases such as boride and sulfocarbide precipitate around the core-shell precipitate.

(3) The segregation of γ'-forming elements results in a γ'-precipitate size gradient between the core and the boundary of the dendrites.

(4) The intrinsic heat treatment inherent to DED elaboration affects the solidified phases and leads to microstructural evolution, especially for the oxides.

This study provides guidelines to appropriately modify the chemical composition of cobalt-based superalloys in order to reduce both segregations and precipitation of undesirable phases. Based on this work, minor changes in chemical composition are possible to design a new alloy resistant to liquid hot cracking during additive manufacturing.

Funding

This work was supported by the French National Research Agency [N° ANR18-LCV1-0004-01] and the Office National d'Etudes et de Recherches Aérospatiales (ONERA).

Acknowledgments

The authors thank Frederic Fossard for the TEM observations and analyses, Jean-Sébastien Mérot (CNRS/ONERA) for site-specific lift-outs excavations and Nicolas Horezan (ONERA) for SEM characterisations. Edouard Chauvet and Arnaud Ferrandez (POLY-SHAPE) are gratefully acknowledged for the fabrication of the samples by DED. Marc Thomas (ONERA) is thanked for the NAFA project management. This work has benefited from the characterization equipment of the Grenoble INP - CMTC platform supported by the Centre of Excellence of Multifunctional Architectured Materials "CEMAM" n°ANR-10-LABX-44-01 funded by the Investments for the Future program.

Declaration of competing interest

The authors declare that they have no known competing financial interests or personal relationships that could have appeared to influence the work reported in this paper.

Data availability

Data available on request from the authors.

References

[1] T. DebRoy, H.L. Wei, J.S. Zuback, T. Mukherjee, J.W. Elmer, J.O. Milewski, A.M. Beese, A. Wilson-Heid, A. De, W. Zhang, Additive manufacturing of metallic components – Process, structure and properties, Prog. Mater. Sci. 92 (2018) 112–224. https://doi.org/10.1016/j.pmatsci.2017.10.001.

[2] J.N. DuPont, J.C. Lippold, S.D. Kiser, Welding Metallurgy and Weldability of Nickel-base Alloys, Wiley–Blackwell, 2009.

[3] J.M. Kalinowski, Weldability of a Nickel-Based Superalloy (NASA Contractor Report 195376), NASA, 1994.

[4] L. Carter, M. Attallah, R. Reed, Laser Powder Bed Fabrication of Nickel-base Superalloys: Influence of Parameters; Characterisation, Quantification and Mitigation of Cracking, in: E.S. Huron, R.C. Reed, M.C. Hardy, M.J. Mills, R.E. Montero, P.D. Portella, J. Telesman (Eds.), Superalloys 2012, 2012: pp. 577–586.

[5] S. Griffiths, H. Ghasemi-Tabasi, A. De Luca, J. Pado, S.S. Joglekar, J. Jhabvala, R.E. Logé, C. Leinenbach, Influence of Hf on the heat treatment response of additively manufactured Ni-base superalloy CM247LC, Mater. Charact. 171 (2021) 110815. https://doi.org/10.1016/j.matchar.2020.110815.

[6] D. Locq, M. Martin, C. Ramusat, F. Fossard, M. Perrut, γ′ Precipitation Study of a Co-Ni-Based Alloy, Metall. Mater. Trans. A. 49 (2018) 3854–3864. https://doi.org/10.1007/s11661-018-4689-x.
[7] R.T. Holt, W. Wallace, Impurities and trace elements in nickel-base superalloys, Int. Met. Rev. 21 (1976) 1–24. https://doi.org/10.1179/imtr.1976.21.1.1.
[8] W. Chen, M.C. Chaturvedi, N.L. Richards, Effect of boron segregation at grain boundaries on heat-affected zone cracking in wrought INCONEL 718, Metall. Mater. Trans. A. 32 (2001) 931–939. https://doi.org/10.1007/s11661-001-0350-0.
[9] A. Després, S. Antonov, C. Mayer, C. Tassin, M. Veron, J.-J. Blandin, P. Kontis, G. Martin, On the role of boron, carbon and zirconium on hot cracking and creep resistance of an additively manufactured polycrystalline superalloy, Materialia. 19 (2021) 101193. https://doi.org/10.1016/j.mtla.2021.101193.
[10] A. De Luca, C. Kenel, S. Griffiths, S.S. Joglekar, C. Leinenbach, D.C. Dunand, Microstructure and defects in a Ni-Cr-Al-Ti γ/γ' model superalloy processed by laser powder bed fusion, Mater. Des. 201 (2021) 109531. https://doi.org/10.1016/j.matdes.2021.109531.
[11] E. Chauvet, P. Kontis, E.A. Jägle, B. Gault, D. Raabe, C. Tassin, J.-J. Blandin, R. Dendievel, B. Vayre, S. Abed, G. Martin, Hot cracking mechanism affecting a non-weldable Ni-based superalloy produced by selective electron Beam Melting, Acta Mater. 142 (2018) 82–94. https://doi.org/10.1016/j.actamat.2017.09.047.
[12] O.A. Ojo, N.L. Richards, K.R. Vishwakarma, Heat-affected zone cracking in nickel-based superalloys and the role of minor elements, in: Weld. Join. Aerosp. Mater., Elsevier, 2021: pp. 199–228. https://doi.org/10.1016/B978-0-12-819140-8.00007-9.
[13] Y.Z. Zhou, A. Volek, Effect of grain boundary fraction on castability of a directionally solidified nickel alloy, Scr. Mater. 54 (2006) 2169–2174. https://doi.org/10.1016/j.scriptamat.2006.02.032.
[14] D. Tomus, P.A. Rometsch, M. Heilmaier, X. Wu, Effect of minor alloying elements on crack-formation characteristics of Hastelloy-X manufactured by selective laser melting, Addit. Manuf. 16 (2017) 65–72. https://doi.org/10.1016/j.addma.2017.05.006.
[15] P. Kontis, E. Chauvet, Z. Peng, J. He, A.K. da Silva, D. Raabe, C. Tassin, J.-J. Blandin, S. Abed, R. Dendievel, B. Gault, G. Martin, Atomic-scale grain boundary engineering to overcome hot-cracking in additively-manufactured superalloys, Acta Mater. 177 (2019) 209–221. https://doi.org/10.1016/j.actamat.2019.07.041.
[16] J. Grodzki, N. Hartmann, R. Rettig, E. Affeldt, R.F. Singer, Effect of B, Zr, and C on Hot Tearing of a Directionally Solidified Nickel-Based Superalloy, Metall. Mater. Trans. A. 47 (2016) 2914–2926. https://doi.org/10.1007/s11661-016-3416-8.
[17] O.A. Ojo, Intergranular liquation cracking in heat affected zone of a welded nickel based superalloy in as cast condition, Mater. Sci. Technol. 23 (2007) 1149–1155. https://doi.org/10.1179/174328407X213323.
[18] S. Sui, J. Chen, X. Ming, S. Zhang, X. Lin, W. Huang, The failure mechanism of 50% laser additive manufactured Inconel 718 and the deformation behavior of Laves phases during a tensile process, Int. J. Adv. Manuf. Technol. 91 (2017) 2733–2740. https://doi.org/10.1007/s00170-016-9901-9.
[19] D. Heydari, A.S. Fard, A. Bakhshi, J.M. Drezet, Hot tearing in polycrystalline Ni-based IN738LC superalloy: Influence of Zr content, J. Mater. Process. Technol. 214 (2014) 681–687. https://doi.org/10.1016/j.jmatprotec.2013.10.001.
[20] R.K. Sidhu, O.A. Ojo, M.C. Chaturvedi, Microstructural Analysis of Laser-Beam-Welded Directionally Solidified INCONEL 738, Metall. Mater. Trans. A. 38 (2007) 858–870. https://doi.org/10.1007/s11661-006-9063-8.

[21] K. Ryou, B. Yoo, P.-P. Choi, On the oxygen-induced hot cracking in a direct laser deposited Ni-based superalloy, Scr. Mater. 196 (2021) 113751. https://doi.org/10.1016/j.scriptamat.2021.113751.
[22] L. Liang, M. Xu, Y. Chen, T. Zhang, W. Tong, H. Liu, H. Wang, H. Li, Effect of welding thermal treatment on the microstructure and mechanical properties of nickel-based superalloy fabricated by selective laser melting, Mater. Sci. Eng. A. 819 (2021) 141507. https://doi.org/10.1016/j.msea.2021.141507.
[23] M. Wen, Y. Sun, J. Yu, J. Meng, S. Wang, Z. Dong, J. Niu, X. Sun, Y. Zhou, Enhancement of multi-pass weld-crack resistance of Co-based superalloys by B-doping, Mater. Charact. 182 (2021) 111527. https://doi.org/10.1016/j.matchar.2021.111527.
[24] Z. Zhou, L. Huang, Y. Shang, Y. Li, L. Jiang, Q. Lei, Causes analysis on cracks in nickel-based single crystal superalloy fabricated by laser powder deposition additive manufacturing, Mater. Des. 160 (2018) 1238–1249. https://doi.org/10.1016/j.matdes.2018.10.042.
[25] S.A. Hosseini, S.M. Abbasi, K.Z. Madar, The effect of boron and zirconium on microstructure and tensile properties of the wrought nickel-based superalloy ATI 718Plus, Mater. Sci. Eng. A. 712 (2018) 780–789. https://doi.org/10.1016/j.msea.2017.12.038.
[26] A. Després, C. Mayer, M. Veron, E.F. Rauch, M. Bugnet, J.-J. Blandin, G. Renou, C. Tassin, P. Donnadieu, G. Martin, On the variety and formation sequence of second-phase particles in nickel-based superalloys fabricated by laser powder bed fusion, Materialia. 15 (2021) 101037. https://doi.org/10.1016/j.mtla.2021.101037.
[27] S.P. Murray, K.M. Pusch, A.T. Polonsky, C.J. Torbet, G.G.E. Seward, N. Zhou, S.A.J. Forsik, P. Nandwana, M.M. Kirka, R.R. Dehoff, W.E. Slye, T.M. Pollock, A defect-resistant Co–Ni superalloy for 3D printing, Nat. Commun. 11 (2020) 4975. https://doi.org/10.1038/s41467-020-18775-0.
[28] T.M. Pollock, A.J. Clarke, S.S. Babu, Design and Tailoring of Alloys for Additive Manufacturing, Metall. Mater. Trans. A. 51 (2020) 6000–6019. https://doi.org/10.1007/s11661-020-06009-3.
[29] H. Park, C. Li, A.E. Jakus, R.N. Shah, H. Choe, D.C. Dunand, High-temperature mechanical properties of γ/γ′ Co–Ni–W–Al superalloy microlattices, Scr. Mater. 188 (2020) 146–150. https://doi.org/10.1016/j.scriptamat.2020.07.009.
[30] S.P. Murray, E.B. Raeker, K.M. Pusch, C. Frey, C.J. Torbet, N. Zhou, S.A.J. Forsik, A.D. Dicus, G.A. Colombo, M.M. Kirka, T.M. Pollock, Microstructure Evolution and Tensile Properties of a Selectively Laser Melted CoNi-Base Superalloy, Metall. Mater. Trans. A. (2022). https://doi.org/10.1007/s11661-022-06716-z.
[31] H. Xu, Y. Zhang, H. Fu, F. Xue, X. Zhou, J. Xie, Effects of boron or carbon on solidification behavior of Co-Ni-Al-W-based superalloys, J. Alloys Compd. 891 (2022) 161965. https://doi.org/10.1016/j.jallcom.2021.161965.
[32] S. Neumeier, L.P. Freund, M. Göken, Novel wrought γ/γ′ cobalt base superalloys with high strength and improved oxidation resistance, Scr. Mater. 109 (2015) 104–107. https://doi.org/10.1016/j.scriptamat.2015.07.030.
[33] NanoMegas, ASTAR, n.d. https://nanomegas.com/tem-orientation-imaging.
[34] E.F. Rauch, M. Véron, Automated crystal orientation and phase mapping in TEM, Mater. Charact. 98 (2014) 1–9. https://doi.org/10.1016/j.matchar.2014.08.010.
[35] Q. Yao, H. Xing, J. Sun, Structural stability and elastic property of the L12 ordered Co3(Al,W) precipitate, Appl. Phys. Lett. 89 (2006) 161906. https://doi.org/10.1063/1.2362574.
[36] M. von Schwarz, O. Summa, Die Kristallstruktur von Tantalkarbid, Met. Met. Met. 12 (1933) 298.
[37] A. Brager, An X-ray examination of titanium nitride III, Acta Physicochim. (1939) 617–632.

[38] Y. Repelin, E. Husson, Etudes structurales d'alumines de transition. I-alumines gamma et delta, Mater. Res. Bull. 25 (1990) 611–621. https://doi.org/10.1016/0025-5408(90)90027-Y.
[39] E. Husson, Y. Repelin, Structural studies of transition aluminas. Theta alumina, Eur. J. Solid State Inorg. Chem. 33 (1996) 1223–1231.
[40] K.R. Whittle, G.R. Lumpkin, S.E. Ashbrook, Neutron diffraction and MAS NMR of Cesium Tungstate defect pyrochlores, J. Solid State Chem. 179 (2006) 512–521. https://doi.org/10.1016/j.jssc.2005.11.011.
[41] O. Ohtaka, T. Yamanaka, S. Kume, Synthesis and X-Ray Structural Analysis by the Rietveld Method of Orthorhombic Hafnia, J. Ceram. Soc. Jpn. 99 (1991) 826–827. https://doi.org/10.2109/jcersj.99.826.
[42] R. Suyama, H. Horiuchi, S. Kume, Structural refinements of ZrO2 and HfO2 treated at 600 C * 6 GPa, Yogyo-Kyokai-Shi. 95 (1987) 567–568.
[43] E. Herlinger, Untersuchungen über die Kristallstruktur von Sesquioxyden und Verbindungen ABO3,. Von W. H. Zachariasen. Skrifter utgitt av Det Norske Videnskap-Akademi i Oslo, I. Mat.-Naturw. Klasse 1928, Nr. 4. Oslo, in Kommission bei J. Dybwad 1928. Kr. 12,—, Z. Für Angew. Chem. 42 (1929) 797–797. https://doi.org/10.1002/ange.19290423015.
[44] J. Yang, Structural analysis of perovskite $LaCr_{1-x}Ni_xO_3$ by Rietveld refinement of X-ray powder diffraction data, Acta Crystallogr. B. 64 (2008) 281–286. https://doi.org/10.1107/S0108768108005739.
[45] R.L. Parker, Zur Kristallstruktur von Anastas und Rutil. (II. Teil. Die Anastasstruktur)., Z. Fuer Krist. Krist. Krist. Krist. -1441977. 59 (1924) 1–54.
[46] E.P. Meagher, G.A. Lager, Polyhedral thermal expansion in the TiO2 polymorphs: Refinement of the crystal structures of rutile and brookite at high temperature, Can. Mineral. 17 (1979) 77–85.
[47] S.F. Bartram, The crystallography of some titanium sulfides, Diss. Abstr. 19 (1958) 1216.
[48] R.W.G. Wyckoff, Crystal structures, Second edition, Interscience Publishers, New York, 1963.
[49] F. Bertaut, P. Blum, Etude des borures de chrome, Comptes Rendus Hebd. Seances Acad. Sci. 1884 - 1965. 236 (1953) 1055–1056.
[50] S.M. Seo, I.S. Kim, J.H. Lee, C.Y. Jo, H. Miyahara, K. Ogi, Eta Phase and Boride Formation in Directionally Solidified Ni-Base Superalloy IN792 + Hf, Metall. Mater. Trans. A. 38 (2007) 883–893. https://doi.org/10.1007/s11661-007-9090-0.
[51] X. Yu, X. Lin, F. Liu, L. Wang, Y. Tang, J. Li, S. Zhang, W. Huang, Influence of post-heat-treatment on the microstructure and fracture toughness properties of Inconel 718 fabricated with laser directed energy deposition additive manufacturing, Mater. Sci. Eng. A. 798 (2020) 140092. https://doi.org/10.1016/j.msea.2020.140092.
[52] Y. Zhang, B. Huang, J. Li, Microstructural Evolution with a Wide Range of Solidification Cooling Rates in a Ni-Based Superalloy, Metall. Mater. Trans. A. 44 (2013) 1641–1644. https://doi.org/10.1007/s11661-013-1645-7.
[53] M.P. Singh, E.F. Olu, P. Pandey, K. Chattopadhyay, Thermophysical and magnetic properties of Co-Ni-Mo-Al-Ta class of tungsten free Co-based superalloys, J. Alloys Compd. (2021) 8. https://doi.org/10.1016/j.jallcom.2021.160379.
[54] N. Wang, S. Mokadem, M. Rappaz, W. Kurz, Solidification cracking of superalloy single- and bi-crystals, Acta Mater. 52 (2004) 3173–3182. https://doi.org/10.1016/j.actamat.2004.03.047.
[55] P. Rong, N. Wang, L. Wang, R.N. Yang, W.J. Yao, The influence of grain boundary angle on the hot cracking of single crystal superalloy DD6, J. Alloys Compd. 676 (2016) 181–186. https://doi.org/10.1016/j.jallcom.2016.03.164.
[56] A. Sonawane, G. Roux, J.-J. Blandin, A. Despres, G. Martin, Cracking mechanism and its sensitivity to processing conditions during laser powder bed fusion of a

structural aluminum alloy, Materialia. 15 (2021) 100976. https://doi.org/10.1016/j.mtla.2020.100976.
[57] I. Lopez-Galilea, C. Zenk, S. Neumeier, S. Huth, W. Theisen, M. Göken, The Thermal Stability of Intermetallic Compounds in an As-Cast SX Co-Base Superalloy: The Thermal Stability of Intermetallic Compounds …, Adv. Eng. Mater. 17 (2015) 741–747. https://doi.org/10.1002/adem.201400249.
[58] S.K. Makineni, M. Lenz, S. Neumeier, E. Spiecker, D. Raabe, B. Gault, Elemental segregation to antiphase boundaries in a crept CoNi-based single crystal superalloy, Scr. Mater. 157 (2018) 62–66. https://doi.org/10.1016/j.scriptamat.2018.07.042.
[59] W. Li, L. Li, S. Antonov, F. Lu, Q. Feng, Effects of Cr and Al/W ratio on the microstructural stability, oxidation property and γ′ phase nano-hardness of multi-component Co–Ni-base superalloys, J. Alloys Compd. 826 (2020) 154182. https://doi.org/10.1016/j.jallcom.2020.154182.
[60] P. Liu, H. Huang, S. Antonov, C. Wen, D. Xue, H. Chen, L. Li, Q. Feng, T. Omori, Y. Su, Machine learning assisted design of γ′-strengthened Co-base superalloys with multi-performance optimization, Npj Comput. Mater. 6 (2020) 62. https://doi.org/10.1038/s41524-020-0334-5.
[61] C.A. Stewart, S.P. Murray, A. Suzuki, T.M. Pollock, C.G. Levi, Accelerated discovery of oxidation resistant CoNi-base γ/γ' alloys with high L12 solvus and low density, Mater. Des. 189 (2020) 108445. https://doi.org/10.1016/j.matdes.2019.108445.
[62] X. Zhuang, S. Antonov, L. Li, Q. Feng, Effect of alloying elements on the coarsening rate of γ' precipitates in multi-component CoNi-based superalloys with high Cr content, Scr. Mater. 202 (2021) 114004. https://doi.org/10.1016/j.scriptamat.2021.114004.
[63] C.C. Silva, H.C. de Miranda, M.F. Motta, J.P. Farias, C.R.M. Afonso, A.J. Ramirez, New insight on the solidification path of an alloy 625 weld overlay, J. Mater. Res. Technol. 2 (2013) 228–237. https://doi.org/doi.org/10.1016/j.jmrt.2013.02.008.
[64] T. Sanviemvongsak, D. Monceau, M. Madelain, C. Desgranges, J. Smialek, B. Macquaire, Cyclic oxidation of alloy 718 produced by additive manufacturing compared to a wrought-718 alloy, Corros. Sci. 192 (2021) 109804. https://doi.org/10.1016/j.corsci.2021.109804.
[65] M. Buttard, B. Chehab, R. Shahani, F. Robaut, G. Renou, C. Tassin, E. Rauch, P. Donnadieu, A. Deschamps, J.-J. Blandin, G. Martin, Multi-scale microstuctural investigation of a new Al-Mn-Ni-Cu-Zr aluminium alloy processed by laser powder bed fusion, Materialia. 18 (2021) 101160. https://doi.org/10.1016/j.mtla.2021.101160.
[66] J. Zhang, R.F. Singer, Hot tearing of nickel-based superalloys during directional solidification, Acta Mater. 50 (2002) 1869–1879. https://doi.org/10.1016/S1359-6454(02)00042-3.
[67] H.-Y. Yan, V.A. Vorontsov, D. Dye, Alloying effects in polycrystalline γ′ strengthened Co–Al–W base alloys, Intermetallics. 48 (2014) 44–53. https://doi.org/10.1016/j.intermet.2013.10.022.
[68] S. Kobayashi, Y. Tsukamoto, T. Takasugi, The effects of alloying elements (Ta, Hf) on the thermodynamic stability of γ′-Co3(Al,W) phase, Intermetallics. 31 (2012) 94–98. https://doi.org/10.1016/j.intermet.2012.06.006.
[69] O. Kubaschewski, C.B. Alcock, Metallurgical Thermochemistry, 5th ed., PERGAMON, 1979.
[70] M.P. Haines, N.J. Peter, S.S. Babu, E.A. Jägle, In-situ synthesis of oxides by reactive process atmospheres during L-PBF of stainless steel, Addit. Manuf. 33 (2020) 101178. https://doi.org/10.1016/j.addma.2020.101178.

[71] B. Zhang, Y. Yu, S. Zhu, Z. Zhang, X. Tao, Z. Wang, B. Lu, Microstructure and wear properties of TiN–Al2O3–Cr2B multiphase ceramics in-situ reinforced CoCrFeMnNi high-entropy alloy coating, Mater. Chem. Phys. 276 (2022) 125352. https://doi.org/10.1016/j.matchemphys.2021.125352.
[72] P. Mair, V.S. Goettgens, T. Rainer, N. Weinberger, I. Letofsky-Papst, S. Mitsche, G. Leichtfried, Laser powder bed fusion of nano-CaB6 decorated 2024 aluminum alloy, J. Alloys Compd. 863 (2021) 158714. https://doi.org/10.1016/j.jallcom.2021.158714.
[73] A. Mitchell, A.J. Schmalz, C. Schvezov, S.L. Cockroft, The Precipitation of Primary Carbides in Alloy 718, in: Superalloys 718 625 706 Var. Deriv. 1994, TMS, 1994: pp. 65–78. https://doi.org/10.7449/1994/Superalloys_1994_65_78.
[74] H.M. Tawancy, N.M. Abbas, A.I. Al-Mana, T.N. Rhys-Jones, Thermal stability of advanced Ni-base superalloys, J. Mater. Sci. 29 (1994) 2445–2458. https://doi.org/10.1007/BF00363439.
[75] N.L. Richards, M.C. Chaturvedi, Effect of minor elements on weldability of nickel base superalloys, Int. Mater. Rev. 45 (2000) 109–129. https://doi.org/10.1179/095066000101528331.
[76] O.A. Ojo, N.L. Richards, M.C. Chaturvedi, Study of the fusion zone and heat-affected zone microstructures in tungsten inert gas-welded INCONEL 738LC superalloy, Metall. Mater. Trans. A. 37 (2006) 421–433. https://doi.org/10.1007/s11661-006-0013-2.
[77] S. Amirabdollahian, F. Deirmina, L. Harris, R. Siriki, M. Pellizzari, P. Bosetti, A. Molinari, Towards controlling intrinsic heat treatment of maraging steel during laser directed energy deposition, Scr. Mater. 201 (2021) 113973. https://doi.org/10.1016/j.scriptamat.2021.113973.
[78] P. Kürnsteiner, M.B. Wilms, A. Weisheit, P. Barriobero-Vila, E.A. Jägle, D. Raabe, Massive nanoprecipitation in an Fe-19Ni-xAl maraging steel triggered by the intrinsic heat treatment during laser metal deposition, Acta Mater. 129 (2017) 52–60. https://doi.org/10.1016/j.actamat.2017.02.069.
[79] A. Després, S. Antonov, C. Mayer, M. Veron, E.F. Rauch, C. Tassin, J.-J. Blandin, P. Kontis, G. Martin, Revealing the true partitioning character of zirconium in additively manufactured polycrystalline superalloys, Addit. Manuf. Lett. 1 (2021) 100011. https://doi.org/10.1016/j.addlet.2021.100011.
[80] K. Persson, Materials Data on HfO2 (SG:61) by Materials Project, (2020). https://doi.org/10.17188/1193253.
[81] K. Persson, Materials Data on HfO2 (SG:14) by Materials Project, (2020). https://doi.org/10.17188/1206948.

6. Supplementary materials

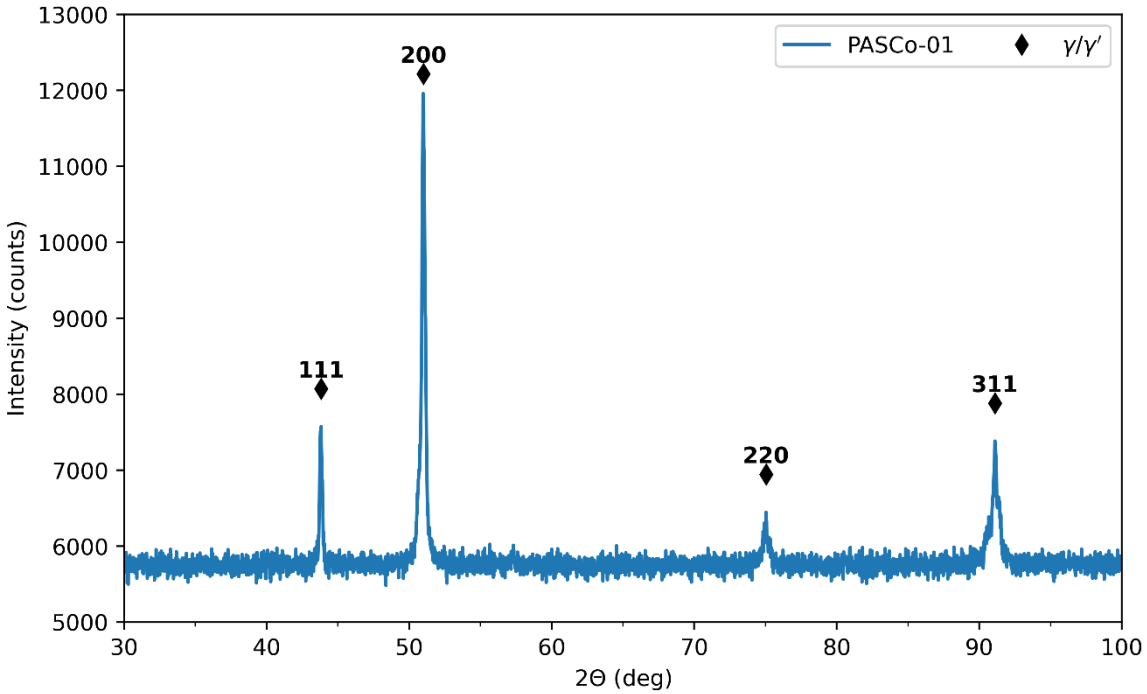

Supplementary figure 1. X-ray diffraction spectra and identified phases of a PASCo-01 as-built sample (Copper source without monochromator, 1/4° slot, 3 hours scanning with a 0.0167 step from 30° to 100°, 45kV, 40mA, EMPYREAN 7 software).

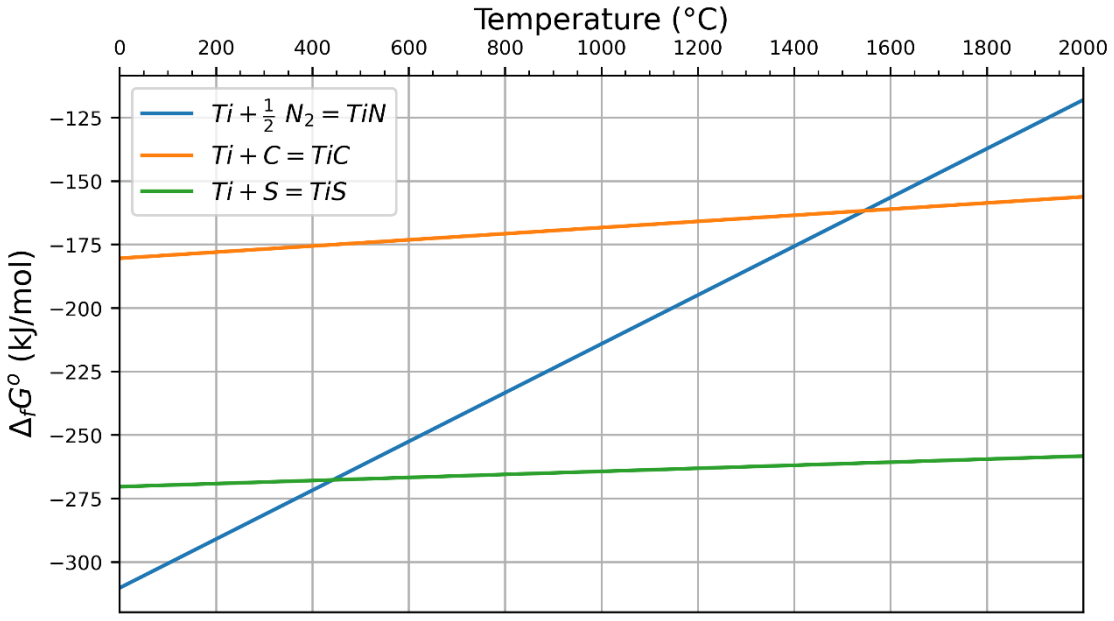

Supplementary figure 2. Ellingham-diagram for the formation of titanium components based on their standard free energy of formation as a function of the temperature [69].

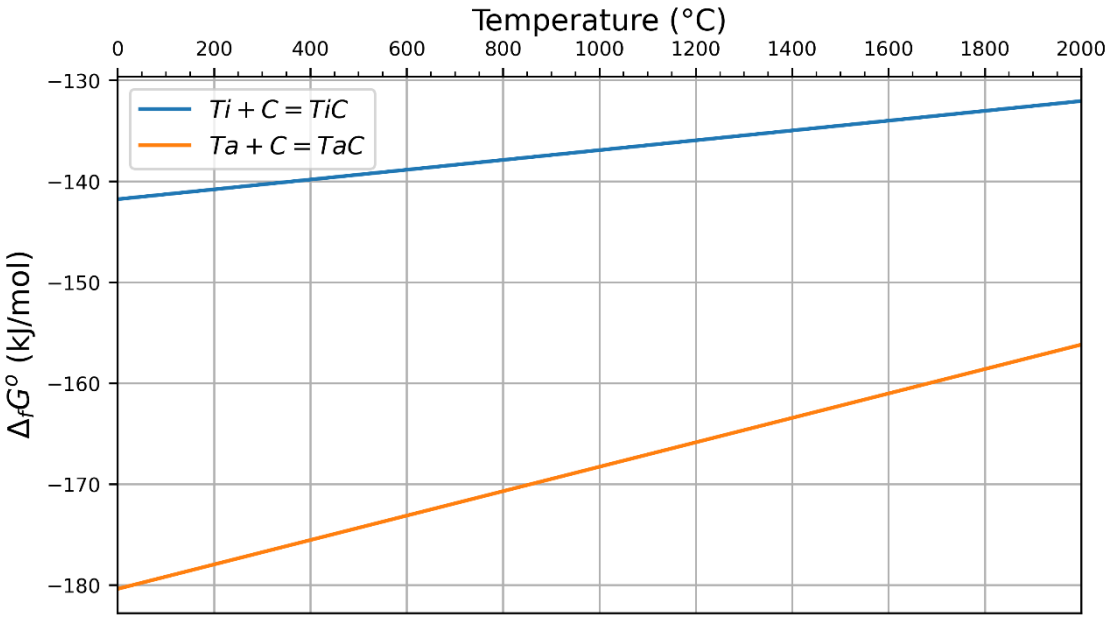

Supplementary figure 3. Ellingham-diagram for the formation of carbides based on their standard free energy of formation depending on the temperature [69].

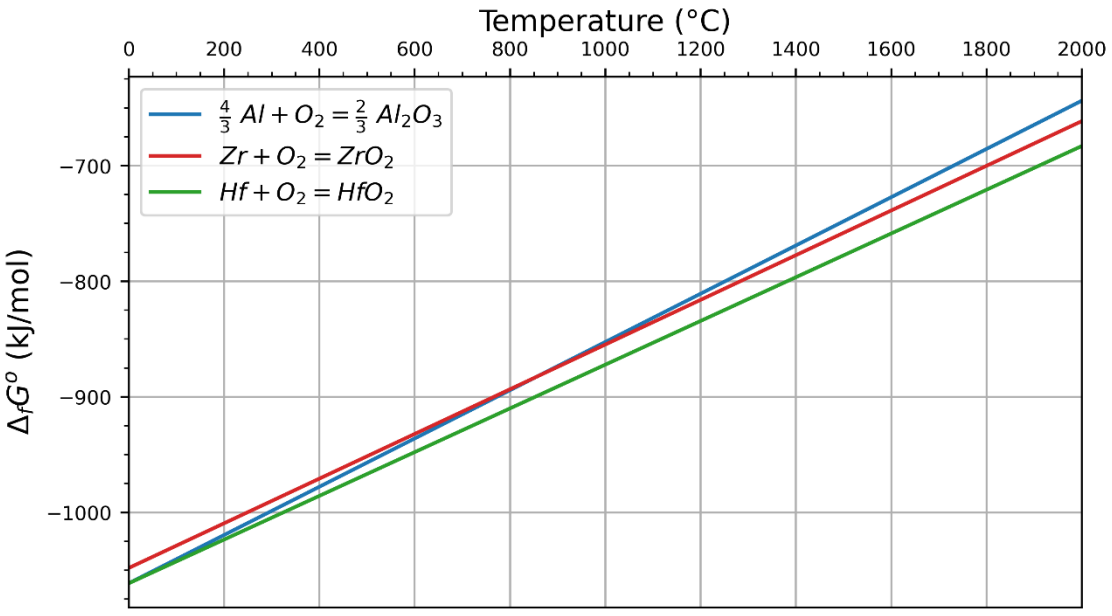

Supplementary figure 4. Ellingham-diagram for the formation of different oxides based on their standard free energy of formation as a function of temperature [69].